ROYAL SOCIETY
OF CHEMISTRY

PAPER

Quantitative, precise and multi-wavelength evaluation of the light-to-heat conversion efficiency for nanoparticular photothermal agents with calibrated photoacoustic spectroscopy†

Théotim Lucas,‡[a,b] Clément Linger, [iD] ‡[a,c] Thomas Naillon, [iD] [d,f]
Mahshid Hashemkhani,[b] Lise Abiven,[b] Bruno Viana,[f] Corinne Chaneac, [iD] [d]
Gautier Laurent, [iD] [e] Rana Bazzi, [iD] [e] Stéphane Roux, [iD] [e] Sonia Becharef,[b]
Giulio Avveduto,[b] Florence Gazeau [iD] [b] and Jérôme Gateau [iD] *[a]

Biomedical photothermal therapy with optical nanoparticles is based on the conversion of optical energy into heat through three steps: optical absorption, thermal conversion of the absorbed energy and heat transfer to the surrounding medium. The light–to–heat conversion efficiency (LHCE) has become one of the main metrics to quantitatively characterize the last two steps and evaluate the merit of nanoparticules for photothermal therapy. The estimation of the LHCE is mostly performed by monitoring the temperature evolution of a solution under laser irradiation. However, this estimation strongly depends on the experimental set-up and the heat balance model used. We demonstrate here, theoretically and experimentally, that the LHCE at multiple wavelengths can be efficiently and directly determined, without the use of models, by calibrated photoacoustic spectroscopy. The method was validated using already characterized colloidal suspensions of silver sulfide nanoparticles and maghemite nanoflowers and an uncertainty of 3 to 7% was estimated for the LHCE determination. Photoacoustic spectroscopy provides a new, precise and robust method of analysis of the photothermal capabilities of aqueous solutions of nanoagents.

1. Introduction

The conversion of optical energy into heat using optically absorbing nanoparticles is the fundamental basis of biomedical photothermal therapy. In addition to the biocompatibility and the ability to target the tissue of interest, specifications of nanoparticles developed as photothermal agents include a strong molar absorption coefficient in the near infra-

[a]*Sorbonne Université, CNRS, INSERM, Laboratoire d'Imagerie Biomédicale, LIB, F-75006 Paris, France. E-mail: jerome.gateau@sorbonne-universite.fr*
[b]*Université Paris Cité, CNRS UMR 7057, Matière et Systèmes Complexes, MSC, F-75006 Paris, France*
[c]*Université Paris-Saclay, CNRS, Institut Galien Paris-Saclay, IGPS, F-91400 Orsay, France*
[d]*Sorbonne Université, CNRS UMR 7574, Laboratoire Chimie de la Matière Condensée de Paris, F-75005 Paris, France*
[e]*Université de Franche-Comté, CNRS, Institut UTINAM, F-25000 Besançon, France*
[f]*Chimie ParisTech, CNRS, PSLResearch University, Institut de Recherche de Chimie Paris, F-75231 Paris, France*
†Electronic supplementary information (ESI) available. See DOI: https://doi.org/10.1039/d3nr03727d
‡These authors contributed equally.

red range (first optical window of biological tissue), a large conversion of the absorbed energy into heat and an efficient transfer of the heat to the surrounding environment. The last two specifications are combined in a metric named the light-to-heat conversion efficiency (LHCE), which is one of the main quantitative figures-of-merit for agents dedicated to photothermal therapy.[1,2] Therefore, a reliable methodology to determine the LHCE of photothermal nanoagents is of interest to compare quantitatively different types of nanoparticles. Of note, the LHCE may vary with the wavelength of the optical excitation and multi-wavelength determination of the LHCE can guide the choice of the laser used for therapeutic applications.

The LHCE is defined in the seminal paper of Roper *et al.*[3] as the fraction of the attenuated light power that is converted into heat flow by the optically absorbing nanoparticles in a solution illuminated with continuous light. The experimental determination of the LHCE by monitoring the temperature evolution of the solution under light irradiation is widespread, but highly challenging. Indeed, the determination of the LHCE value requires an equation modelling the heat balance in the experimental configuration, and a considerable varia-

bility is observed between the different models proposed previously.[4] Based on a critical analysis of the different pre-existing models, Paściak *et al.*[4] proposed a standardized method that can be considered as the state-of-the-art for the LHCE evaluation relying on the monitoring of the temperature evolution of a solution under light irradiation. However, this LHCE determination method suffers from a large uncertainty (~39%) and tedious and long experimental procedures when the evaluation is required at several excitation wavelengths. Various particles were characterized by this method and at different wavelengths,[2] which provide a reference dataset for the present study.

Alternatively, other physical principles have been investigated to determine the LHCE. For graphene nanoparticles, Savchuk *et al.*[5] computed the LHCE using only measurements of the optical absorption. The light power absorbed by the laser-irradiated solution was measured using a power meter and an integrating sphere. However, the method assumes that all the absorbed energy is transformed into heat, which may be true for graphene but is not valid for luminescent particles for instance. Recently, Gu and Zhong[1] reported LHCE evaluation based on a photothermal and electrothermal equivalence (PEE) method consisting in the measurement of the heat dissipation coefficient of a sample under electric heating. They demonstrate that the LHCE value deduced from electrothermal method is equal to that obtained with laser heating for the same temperature rise. However, the method can only be applied with dry solid materials and not solutions, which can cause sample modification during the drying process. Moreover, the heat transfer from the agent to the surrounding medium may be different for dry materials and not applicable to photothermal therapy in biological tissue.

We propose here a new LHCE determination method based on the fact that particles considered as photothermal nanoagents are also contrast agents for photoacoustic imaging.[6,7] Indeed, the photoacoustic effect combines the conversion of optical energy into heat (a process that is common with photothermal therapy) with the conversion of heat into pressure and subsequently ultrasound waves. The optical excitation in photoacoustic imaging is performed with nanosecond pulses. As the thermal relaxation time of the solution compartment (>17 ms for an aqueous solution in a compartment with linear dimension >0.1 mm) is much larger than the temporal duration of the optical pulse, the heat transport outside the solution compartment can be ignored during the ultrasound generation. This condition is called thermal confinement. Due to thermal confinement, no model of heat balance is needed for the illuminated solution. Moreover, for gold nanospheres, Prost *et al.*[8] demonstrated that, on a nanometric scale and in the nanosecond regime, the ultrasound generation is almost entirely due to the water layer surrounding the particle (layer thickness ~50 nm for 8 ns pulses). Therefore, the photoacoustic generation is sensitive to the heat transfer from the particle to the solvent, but it is not sensitive to the macroscopic heat transfer from the heated solution to its environment. Recently, we have developed a calibrated photoacoustic spectrometer[9]

that enables to convert the amplitude of the photoacoustic signals generated by a aqueous suspension of nanoparticles into spectroscopic units. The evaluated photoacoustic coefficient corresponds to the optical absorption coefficient restricted to the absorption effectively transferred into heat to the surroundings of the nanoagent and corrected for the potentially modified conversion of the heat into pressure compared to water (Grüneisen coefficient).[9]

In this paper, we develop the theoretical framework supporting that the LCHE can be obtained by computing the ratio of the photoacoustic coefficient of a solution measured with quantitative photoacoustic spectroscopy and the attenuation coefficient obtained by standard transmission spectrophotometry of the same solution. We validate experimentally our innovative method by measuring the LHCE over a broad range of optical wavelengths (680 nm–920 nm) for two classes of colloidal nanoparticles: semiconductor (silver sulfide nanoparticles) and metal oxide (maghemite nanoflowers). The LHCE values of these nanoagents were already measured by Paściak *et al.*[2] by another method allowing to compare and discuss our results.

2. Results and discussion

2.1. Theoretical framework for the determination of the LHCE with quantitative photoacoustic spectroscopy

Photothermal therapy and photoacoustic ultrasound generation both rely on the conversion of the absorbed optical energy into heat. First, we mathematically link the equations of the two modalities to compute the LHCE and give the experimental limits underlying the applicability of these equations and of our approach. The equations are valid for molecular solutions and colloidal suspensions. For the sake of clarity, we will consider that the mixture is a colloid and the terms dispersed phase and continuous phase are used to refer to the solid nanoparticles and the liquid medium in which they are dispersed, respectively.

2.1.1. Light-to-heat conversion efficiency: photothermal model. The LHCE, notated η_T, is defined in the seminal paper of Roper *et al.*[3] by the eqn (1) which relates the laser-induced rate of heat flow $\dot{Q}_I$ and the optical attenuation A_λ induced by the dispersed phase for a solution illuminated by a laser at the optical wavelength λ.

$$\dot{Q}_I = I_0 \cdot (1 - 10^{-A_\lambda}) \cdot \eta_T \tag{1}$$

with I_0 the incident laser radiant power (in W) on the solution. This formula derives from the attenuation measurements in transmission spectrophotometry. Therefore, it corresponds to a macroscopic scale configuration, typically a cuvette filled with a solution and illuminated from one side. Moreover, it assumes a unidirectional propagation of the laser beam though the solution and describes a global energy balance using the difference between the incident laser radiant power I_0 and the transmitted laser radiant power in this propagation direction $I_0 \times 10^{-A_\lambda}$. We note that both the absorption and the

scattering of the solution can influence the unidirectional transmitted laser radiant power when measured by the attenuation A_λ. Moreover, the contribution of the continuous phase to the attenuation is implicitly neglected in this formula as the attenuation is measured with a spectrophotometer and a blank measurement with the continuous phase alone.

To link the photothermal and photoacoustic equations, we derive again the energy balance at mesoscopic scale and perform an integration to the macroscopic scale (see ESI†). For the sake of simplicity, a single kind of absorber is considered given that the generalization to multiple kinds of absorbers can be performed by applying the Beer–Lambert–Bouguer law. We introduce the photothermal conversion efficiency $E_{pt}(\lambda)$, which is the ratio of the energy effectively converted into a thermal increase of the solution to the total absorbed optical energy. E_{pt} may be inferior to 1, due to various competitive deexcitation pathways such as fluorescence or photochemical reactions, for instance. We demonstrate that the LHCE is actually the product of the photothermal conversion efficiency $E_{pt}(\lambda)$ of the dispersed phase (unit less) and the ratio between the absorption coefficient of the dispersed phase $\mu_a(\lambda)$ (in m^{-1}) and the attenuation coefficient of the solution $\mu_{att, solution}(\lambda)$ (in m^{-1}):

$$\eta_T(\lambda) = E_{pt}(\lambda) \cdot \frac{\mu_a(\lambda)}{\mu_{att, solution}(\lambda)}. \tag{2}$$

As the attenuation coefficient combines the absorption coefficient and the scattering coefficient, eqn (2) shows that the scattering properties of the solution influence the LHCE. In contrast, $E_{pt}(\lambda)$ exclusively refers to the absorbed optical energy transformed into heat.

2.1.2.   Validity limits of the LHCE as an intrinsic figure-of-merit. A question arises from eqn (2): is the LHCE an intrinsic property of an absorber or does it depend on its concentration in the solution (regardless of the potential coupling or aggregation phenomena of the optical absorbers)?

For a non-scattering solution, $\mu_{att, solution}(\lambda) = \mu_a(\lambda) + \mu_{a, continuous}(\lambda)$ with $\mu_{a, continuous}$ the absorption coefficient of the continuous phase (in m^{-1}). Therefore, η_T equals E_{pt} and the LHCE can effectively be considered has an intrinsic property of the absorber, if the absorption coefficient of the continuous phase can be neglected compared to the dispersed phase. Since $\mu_a(\lambda)$ is proportional to the concentration of the dispersed phase according to the Beer–Lambert–Bouguer law, a sufficient concentration needs to be reached to neglect the absorption of the continuous phase. For molecular absorbers usually used in biomedical application,[10] micromolar to millimolar concentration would be sufficient since the molar absorption coefficient is on the order of 10^4 to 10^5 cm^{-1} M^{-1}, while the decadic absorption coefficient of water[11] in the near infrared (NIR) $\mu_{a, water}(\lambda)/\ln(10)$ varies from 2×10^{-3} cm^{-1} at $\lambda = 690$ nm to 5×10^{-2} cm^{-1} at 920 nm.

For scattering agents like nanoparticles, the Beer–Lambert–Bouguer law assumes a linear dependence of the absorption and attenuation coefficients with the concentration of agents, and can be considered valid for samples with a small volume fraction of absorbers and a limited slab thickness.[12] For nanoparticular agents (order of 100 nm diameter), the volume fraction of the dispersed phase can be considered negligible with regards to the continuous phase at concentrations from tens or hundreds nanomolar. Given that the molar absorption coefficient of nanoagents is a few orders of magnitude higher than for molecular agents, the absorption coefficient of the continuous phase can be neglected compared to the dispersed phase at this particle concentration, and the ratio $\mu_a(\lambda)/\mu_{att, solution}$ can be considered independent from the concentration.

In sum, the light-to-heat conversion efficiency defined by eqn (1) and (2) can be considered to be an intrinsic property of non-scattering and scattering agents for concentrations ensuring an absorption much higher than the continuous phase and a negligible volume fraction of the dispersed phase.

2.1.3.   Spectrophotometric determination of $\mu_{att, dispersed}(\lambda)$. The attenuation coefficient of the dispersed phase $\mu_{att, dispersed}$ can be directly evaluated with a spectrophotometer in transmission mode. A sample thickness L inferior to $1/\mu_{att, solution}(\lambda)$ ensures measurement in a single optical scattering regime.

$$\mu_{att, dispersed}(\lambda) = \frac{A_\lambda}{L} \cdot \ln(10) \tag{3}$$

where A_λ is the attenuation measured with a spectrophotometer and a blank measurement with the continuous phase. A_λ is abusively called absorbance in spectrophotometry operating in transmittance.

2.1.4.   Photoacoustic determination of $E_{pt}(\lambda) \cdot \mu_a(\lambda)$. For the evaluation of $E_{pt}(\lambda) \cdot \mu_a(\lambda)$, we propose to use a recently developed method, the calibrated photoacoustic spectroscopy.[9] In this photoacoustic method, the optically absorbing solution is inserted in PTFE tubes with an inner diameter of 0.2 mm. The tubes are immersed in a water bath maintained at a constant temperature, they are illuminated with nanosecond laser pulses, and for each laser pulse, the heating and subsequent thermo-elastic expansion of the illuminated solution generate ultrasound waves. The generated ultrasound waves are then recorded by an ultrasound detector.

For a tube filled with a solution and illuminated with a laser pulse at the optical wavelength λ, the contribution of the optically absorbing dispersed phase to the ultrasound signal detected at the relative position r_i is equal to (see ESI†):

$$s_i^{dispersed}(t, \lambda) = E_{pt}(\lambda) \cdot \mu_a(\lambda) \cdot \Gamma_{solution} \cdot \chi^{in\ tube}(r_i, t, \lambda) \tag{4}$$

where t is the time and $\chi^{in\ tube}(r_i, t, \lambda)$ is the ultrasound waveform that incorporates the temporal response of the detector, the temporal profile of the optical excitation and its amplitude inside the tube, and the spatial response of the detector to the inside of the tube. $\Gamma_{solution}$ is the dimensionless Grüneisen coefficient of the solution. This coefficient describes the conversion of the heat energy to the initial pressure rises resulting in the ultrasound waves.

To extract $s_i^{dispersed}(t, \lambda)$ from the recorded ultrasound signal, we subtract the ultrasound signal measured by the

detector for the tube filled with the continuous phase from the signal measured for the tested solution. This is equivalent to the blank acquisition in spectrophotometry. The ultrasound detector has a linear response. Therefore, this subtraction removes the contribution of the bath water outside the tube and the tube itself. It also removes the contribution of the continuous phase inside the tube to obtain $s_i^{\text{dispersed}}(t,\lambda)$ if two conditions are satisfied: (1) the illumination inside the tube can be considered constant regardless of the solution inside the tube, and (2) the Grüneisen coefficient of the solution is equal to the Grüneisen coefficient of the continuous phase. For a tube diameter of $D_{\text{tube}} = 0.2$ mm, the first condition implies that the attenuation coefficient of the solution $\mu_{\text{att, solution}}$ has to be small compared to: $1/D_{\text{tube}} = 50$ cm^{-1}. In the current study, we limited the attenuation coefficient to 7 cm^{-1}. For the second condition, it has been shown that, for gold nanospheres illuminated in the nanosecond pulsed regime, the photoacoustic pressure arises from the layer of continuous phase surrounding the heated nanoparticles.[8,13] This is true in particular when the thermal volume expansion coefficient of the particles can be considered much lower than that of the continuous phase, and that the mass fraction of the dispersed phase can be considered small. For molecular absorbers and for solid nanoparticles, we assume here that ultrasound emission arises dominantly from the continuous phase and therefore the thermodynamic properties of the continuous phase should be considered for the Grüneisen coefficient. Consequently, $\Gamma_{\text{solution}} \approx \Gamma_{\text{continuous}}$.

From $s_i^{\text{dispersed}}(t,\lambda)$ measured over an array of ultrasound detectors, the photoacoustic coefficient $\theta^{\text{PA}}(\lambda)$ for the solution of absorbers[9] is then assessed.

$$\theta^{\text{PA}}(\lambda) = E_{\text{pt}}(\lambda) \cdot \mu_{\text{a}}(\lambda) \cdot \frac{\Gamma_{\text{continuous}}}{\Gamma_{\text{water}}} \quad (5)$$

In brief, signals $s_i^{\text{dispersed}}(t,\lambda)$ measured with the detector array are projected in an image space to increase the signal-to-noise ratio and the amplitude of the signal is extracted to obtain $A^{\text{PA}}(\lambda)$, which is proportional to $\theta^{\text{PA}}(\lambda)$. Then, two reference solutions are used to calibrate the photoacoustic spectrometer. Both solutions are non-scattering, implying that $\mu_{\text{a}}(\lambda)$ can be measured by spectrophotometry. Additionally, the reference solutions are assumed to have a photothermal coefficient E_{pt} equal to one. Indeed, the reference optical absorbers have no other deexcitation pathway since they do not have any fluorescence properties nor induce photochemical reaction. The first reference solution, cupric sulfate $CuSO_4 \cdot 5H_2O$ (0.25 M or 62.4 g L^{-1}), has a strong absorption all over the investigated wavelength range (680 nm–920 nm), but it has a higher Grüneisen coefficient than water. This solution is used to obtain the per-wavelength calibration. The second reference solution is obtained by mixing nigrosine powder with water (173 mg L^{-1}) and can be considered to have the Grüneisen coefficient of water. However, its absorption coefficient is decaying over the investigated wavelength range. This second solution is used to obtain a global calibration to the Grüneisen coefficient of water Γ_{water}. With the photoacoustic coefficient,

we can compute a Light-to-Photoacoustic Conversion Efficiency (LPCE):

$$\eta_{\text{PA}}(\lambda) = \frac{\theta^{\text{PA}}(\lambda)}{\mu_{\text{att, dispersed}}(\lambda)}$$
$$= E_{\text{pt}}(\lambda) \cdot \frac{\mu_{\text{a}}(\lambda)}{\mu_{\text{att, dispersed}}(\lambda)} \cdot \frac{\Gamma_{\text{continuous}}}{\Gamma_{\text{water}}}. \quad (6)$$

The LPCE is different from the photoacoustic generation efficiency defined elsewhere.[9] Indeed, the LPCE is the ratio of the photoacoustic coefficient to the attenuation coefficient of the dispersed phase $\mu_{\text{att, dispersed}}(\lambda)$, while the photoacoustic generation efficiency is the ratio of the photoacoustic coefficient to the absorption coefficient $\mu_{\text{a}}(\lambda)$. Therefore, the LCPE is sensitive to the scattering coefficient of the dispersed phase.

When the attenuation of the solution is dominated by the dispersed phase, the LPCE can be linked to the LHCE according to:

$$\eta_{\text{PA}}(\lambda) = \eta_{\text{T}}(\lambda) \cdot \frac{\Gamma_{\text{continuous}}}{\Gamma_{\text{water}}}. \quad (7)$$

2.1.5. LHCE computed with the photoacoustic coefficient. For an aqueous colloidal suspension, for which the Grüneisen coefficient equals that of the water – *i.e.* the thermal volumetric expansion of the dispersed phase can be neglected and the photoacoustic generation arises from layers with thermodynamic properties of water-, eqn (7) leads to a determination of the light-to-heat conversion efficiency from the photoacoustic coefficient and attenuation coefficient of the dispersed phase:

$$\eta_{\text{T}}(\lambda) \cong \eta_{\text{PA}}(\lambda) = \frac{\theta^{\text{PA}}(\lambda)}{\mu_{\text{att, dispersed}}(\lambda)}. \quad (8)$$

The method of determination of the LHCE with calibrated photoacoustic spectroscopy is schematically illustrated and summarized in Fig. 1.

2.2. Multiwavelength experimental determination of the LHCE for colloidal suspensions of nanoparticles

We considered here solutions of solid nanoparticles dispersed in purified water. The thermal volumetric expansion coefficients of the particles are neglected, and we assume that the photoacoustic generation arises from the layer of water surrounding the particles. Therefore, the LHCE can be considered equal to the LPCE. For a straight comparison with the results of Paściak *et al.*,[2] we used nanoparticles synthesized by the same research teams and with the same protocols, but new batches were prepared.

2.2.1. Silver sulfide nanoparticles synthesized at low AgNO₃ concentration. Among the silver sulfide (Ag_2S) particles investigated by Paściak *et al.*,[2] we chose particles with two different coatings: mercaptoundecanoic acid (Ag_2S@MUA) and dithiolated diethylenetriamine pentaacetic acid (Ag_2S@DTDTPA). These particles, synthetized similarly to the particles reported in ref. 2, are referred as Ag_2S particles prepared from a low concentration of AgNO₃ (5 mM). At a wave-

Fig. 1 Experimental method proposed for the determination of the light-to-heat conversion efficiency using photoacoustic spectrometry and absorbance spectrophotometry of a given aqueous suspension of nanoparticles. For the photoacoustic spectrometer, the sample is placed in a tube and illuminated with pulsed light. The amplitude of the ultrasound (US) wave generated with the photoacoustic effect is measured from the signal captured with an US detector. This ultrasound amplitude is converted in the photoacoustic coefficient θ^{PA} thanks to a calibration process. For the absorbance spectrophotometer, the sample is placed in a cuvette of known path length and illuminated by continuous light. The ratio of the transmitted light power and the incident light power measures the transmittance, that can be converted in the attenuation coefficient. Both spectrometers are blanked with the continuous phase, this leads to obtain coefficients for the dispersed phase. The light-to-photoacoustic conversion efficiency η_{PA} is then obtained from the ratio between the photoacoustic coefficient and the attenuation coefficient. When the Grüneisen coefficient of the solution can be assumed to be the Grüneisen coefficient of water, η_{PA} equals η_T the light-to-heat conversion efficiency, LHCE.

length of 794 nm, the LHCE has been evaluated by Paściak et al.[2] using a photothermal measurement to be of 83% and 79% for Ag$_2$S@MUA$_{low}$ and Ag$_2$S@DTDTPA$_{low}$, respectively. Moreover, for Ag$_2$S@DTDTPA$_{low}$, the LHCE has been evaluated[2] to be above 90% at 808 nm and even above 100% for 940 nm.

Fig. 2 presents the photoacoustic spectra and the attenuation spectra of the two compounds as well as their ratio η_{PA} in the range 680–920 nm with an evaluation every 10 nm. Experiments were performed on the same 1 mL volume of colloidal suspension. The precision of determination of the LPCE was found on the order of ±4% for Ag$_2$S@MUA$_{low}$ and for Ag$_2$S@DTDTPA$_{low}$.

The LPCE can be considered constant with no dependence on the wavelength for Ag$_2$S@MUA$_{low}$ (Fig. 2(b)) with an average value of 100%. This result is confirmed by the match between the photoacoustic spectra and the attenuation spectra in Fig. 2(a). Identifying the LPCE and the LHCE, this result indicates that all the absorbed optical energy is converted into heat and that the scattering of the solution can be neglected. Such total conversion of optical energy into heat is in line with the low quantum yield of this agent, which is measured to be equal to 1.9%. For Ag$_2$S@DTDTPA$_{low}$, the photoacoustic coefficients were found lower than the attenuation coefficients (Fig. 2(c)) in the range of 680–920 nm. More quantitatively, the determined LPCE values are between 65% and 82% with a mean value of 74% in the range of 680–920 nm, continuously decreasing by 10% between 680 nm and 780 nm (Fig. 2(d)). The quantum yield could not be determined on this sample but a low quantum yield (<1%) was reported in ref. 2 and a low fluorescence signal was measured here. Thus, the photother-
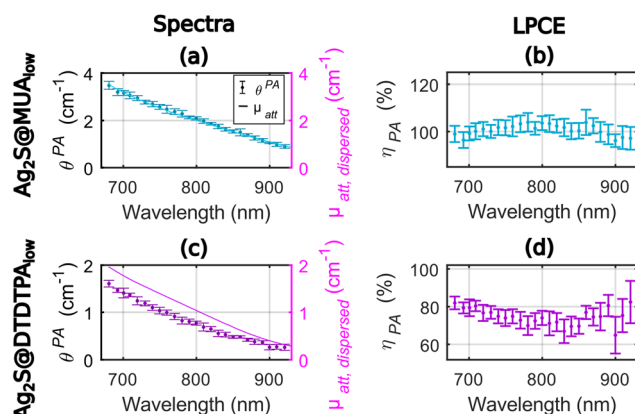

Fig. 2 Photoacoustic (right) and attenuation (left) spectra ((a) and (c)) and Light-to-Photoacoustic Conversion Efficiency (LPCE, (b) and (d)) for the silver sulfide (Ag$_2$S) nanoparticles prepared with low concentration of AgNO$_3$ for two different coatings: mercaptoundecanoic acid (Ag$_2$S@MUA$_{low}$) and dithiolated diethylenetriamine pentaacetic acid (Ag$_2$S@DTDTPA$_{low}$), respectively. The photoacoustic coefficients θ^{PA} were obtained with a calibrated photoacoustic spectrometer. Here, θ^{PA} is assumed to be equal to the photothermal conversion efficiency multiplied by the absorption coefficient of the dispersed phase. The attenuation coefficient $\mu_{att,\ dispersed}(\lambda)$ is measured with a spectrophotometer. The LPCE is the ratio of θ^{PA} to $\mu_{att,\ dispersed}(\lambda)$. For the photoacoustic coefficients, the median $\pm$ median absolute deviation values were displayed with dot markers and error bars. For the LPCE, the error bars correspond to the relative uncertainty and consider all the measurement and calibration steps. The axis ranges for the LCPE were 40% and 50% for (b) and (d), respectively.

mal conversion efficiency $E_{pt}(\lambda)$ is expected to be equal to 1 and the fluorescence properties cannot explain the lower LPCE compare to Ag₂S@MUA$_{low}$. On the other hand, the small size (∼2.3 nm on the TEM images (Fig. S2.b†), the hydrodynamic size could not be determined properly) of Ag₂S@DTDTPA$_{low}$ particles does not call for a large scattering. However, the large DTDTPA ligand combined with the low absorption of the particles could result in a larger relative contribution of the scattering to $\mu_{att,\ dispersed}(\lambda)$ for Ag₂S@DTDTPA$_{low}$ compared to Ag₂S@MUA$_{low}$ and could account for the difference in the LPCE. The scattering is expected to be larger at shorter wavelengths which agrees with the decreasing difference $\mu_{att,\ dispersed}(\lambda) - \theta^{PA}(\lambda)$ with the increasing wavelength (Fig. 2(c)).

The difference in the LHCE values for the two Ag₂S agents are larger at 790 nm (∼30%) than in the study of Paściak *et al.*[2] (4%). However, the variation of the LHCE with the optical wavelength is smoother for Ag₂S@DTDTPA$_{low}$ and the LHCE uncertainty of our method is only of 4% here compare to 39% in the photothermal evaluation of Paściak *et al.*[2] A LHCE of 100% ± 4% for Ag₂S@MUA$_{low}$ is also consistent with LHCE of 93% ± 8% at 808 nm reported by Shen *et al.*[14] by monitoring of the temperature of a laser illuminated solution of PEG-coated silver sulfide nanoparticles with a quantum yield below 1%.

2.2.2. Silver sulfide nanoparticles synthesized at high AgNO₃ concentration. In addition, Ag₂S particles synthesized from a high concentration of AgNO₃ equal to 20 mM, and the same two different coatings, were investigated: Ag₂S@MUA$_{high}$ and Ag₂S@DTDTPA$_{high}$.

As shown in Fig. 3, the photoacoustic coefficients were found lower than the attenuation coefficients for Ag₂S@MUA$_{high}$ (Fig. 3(a)) and the LPCE of Ag₂S@MUA$_{high}$ was determined to be almost constant (Fig. 3(b)) in the range of 680–850 nm (68% ± 2% average ± std). For this sample, the quantum yield was measured to be 28%, which implies that $E_{pt} \leq 72\%$ and can explain the difference of LPCE value compare to Ag₂S@MUA$_{low}$. The LPCE of Ag₂S@DTDTPA$_{high}$ was found equal to 100% (Fig. 3(d)), while the quantum yield was found equal to 1.6%. The intensity based hydrodynamic size of Ag₂S@DTDTPA$_{high}$ was 421 nm whilst it was measured equal to 168 nm for Ag₂S@MUA$_{high}$. These data clearly showed that the higher scattering of light due to the presence of large Ag₂S@DTDTPA$_{high}$ nanoparticles was counterbalanced by the large contribution of the absorption to the attenuation and did not lead to a LPCE below 100%. One can note that the much higher absorbance of Ag₂S@DTDTPA$_{high}$ compare to Ag₂S@DTDTPA$_{low}$ could explain that the scattering is negligible in the attenuation coefficient of this sample, besides the larger size of the particles. The precision of determination of the LPCE was found on the order of ±4% for Ag₂S@MUA$_{high}$ and for Ag₂S@DTDTPA$_{high}$.

In sum for the silver sulfide nanoparticles, the LPCE could determine a LHCE compatible with the quantum yield of the samples. A LHCE of 100% ± 4% was determined for the samples with a quantum yield lower than 2% and a large optical absorption. Additionally, the LPCE of 68% ± 4% for Ag₂S@MUA$_{high}$ is consistent with the 28% quantum yield. We could also determine

Fig. 3 Photoacoustic and attenuation spectra ((a) and (c)) and Light-to-Photoacoustic Conversion Efficiency (LPCE, (b) and (d)) for the silver sulfide (Ag₂S) prepared with a high concentration of AgNO₃ and with two different coatings: Ag₂S@MUA$_{high}$ and Ag₂S@DTDTPA$_{high}$, respectively. The photoacoustic coefficients θ^{PA} were obtained with a calibrated photoacoustic spectrometer. Here, θ^{PA} is assumed to be equal to the photothermal conversion efficiency multiplied by the absorption coefficient of the dispersed phase. The attenuation coefficient $\mu_{att,\ dispersed}(\lambda)$ is measured with a spectrophotometer. The LPCE is the ratio of θ^{PA} to $\mu_{att,\ dispersed}(\lambda)$. For the photoacoustic coefficients, the median ± median absolute deviation values were displayed with dot markers and error bars. For the LPCE, the error bars correspond to the relative uncertainty and consider all the measurement and calibration steps. The axis ranges for the LCPE were 40%.

that, for particles with a significant absorption, the influence of the scattering can be neglected while it results in a lower LPCE for Ag₂S@DTDTPA$_{low}$. The LHCE values determined with our photoacoustic method are consistent with the values determined by Paściak *et al.* if we consider the large uncertainty of their method and the batch-to-batch variability. Importantly, our photoacoustic method gives access to physical explanations for the LHCE comparison for different materials, particularly the role of fluorescence and scattering properties of the solution, that were not accessible with Paściak *et al.*'s photothermal method. In addition, the photoacoustic evaluation allows for a spectral and monotonous determination of the LHCE over a large wavelength range providing unprecedented information on the spectral dependence of the LHCE.

2.2.3. Maghemite nanoflowers. We chose to determine the LHCE of the same metal oxide nanoparticles as Paściak *et al.*:[2] maghemite nanoflowers (γ-Fe₂O₃) and the same maghemite nanoflowers decorated with gold nanoparticles (γ-Fe₂O₃–Au). These two nanostructures have been developed for targeted magnetothermal and photothermal therapy of fibrotic tumors.[15] The two samples were measured at the same mass concentration of iron 1.67 g Fe L⁻¹. Additionally, we performed measurements for the gold nanoparticles (Au NP, core size of 2.3 nm ± 0.3 nm, hydrodynamic diameter of 8.3 nm ± 2.1 nm) used to decorate the nanoflowers but at a concentration in gold 3.5 times larger than in the solution of γ-Fe₂O₃–Au. γ-Fe₂O₃ had a citrate coating (hydrodynamic diameter of 45.0 nm ± 0.5 nm), while the gold nanoparticles were coated with DTDTPA (alone or when decorating the

nanoflower). While γ-Fe₂O₃ and γ-Fe₂O₃–Au have a similar size determined from the TEM images (41.1 ± 4 nm and 42.9 ± 4 nm, respectively), γ-Fe₂O₃–Au has a hydrodynamic diameter of 81.1 nm ± 0.8 nm. The higher value of hydrodynamic diameter observed for γ-Fe₂O₃–Au cannot be explained only by the presence of Au NP and may result from partial agglomeration of the colloidal particles. The LHCE had been evaluated by Paściak *et al.*[2] to be equal to 82% and 86% at a wavelength of 794 nm for γ-Fe₂O₃ and γ-Fe₂O₃–Au, respectively, with non-monotonous variations between 80% and 110% in the range 668–940 nm for both particles.

Fig. 4 displays the photoacoustic spectra and the attenuation spectra of the three compounds and η_{PA} in the range 680–920 nm. For γ-Fe₂O₃, the LPCE was determined to be around 100% with a slight increase (+4%) in the range 680–780 nm that may be due to a weak scattering of the solution at shorter wavelength (Fig. 4(b)). For Au NP, the photoacoustic and attenuation spectra were superimposed, leading to a constant LPCE equal to 100% (Fig. 4(c) and (d)). The precision of determination of the LPCE was found on the order of ±3% (mean value) for γ-Fe₂O₃ and Au NP. The LHCE of 100% for γ-Fe₂O₃, obtained with our photoacoustic method, is consistent with the fact that the particles are not luminescent and only weakly scattering.

For γ-Fe₂O₃–Au, the attenuation and photoacoustic spectra have different shapes (Fig. 4(e)) with a much larger difference $\mu_{att,\ solute}(\lambda) - \theta^{PA}(\lambda)$ at shorter wavelengths. Interestingly the photoacoustic spectrum of the γ-Fe₂O₃–Au sample could be decomposed in a linear sum of the photoacoustic spectra of γ-Fe₂O₃ and Au NP samples with weights 0.79 and 0.29, respectively (see Fig. S4†). However, the attenuation spectrum could be decomposed in a linear sum of the attenuation spectra of the γ-Fe₂O₃ and Au NP samples with weights 0.71 and 0.52, respectively. The weights for γ-Fe₂O₃ are close for both the attenuation and the photoacoustic spectra. The weight for the Au NP sample corresponds to the difference in the gold concentration between the colloidal suspensions of Au NP and γ-Fe₂O₃–Au for the photoacoustic spectrum. The much larger weight of Au NP for the attenuation spectrum could be attributed to the enhanced scattering at the shorter wavelengths of the bimetallic hybrid nanostructures γ-Fe₂O₃–Au in comparison to their individual constituents γ-Fe₂O₃ and Au NP. Indeed, the larger hydrodynamic diameter of the γ-Fe₂O₃–Au particles implies a larger scattering and the exponentially decaying shape of the attenuation spectrum of Au NP in the range 680–920 nm is also typical from what would be expected for scattering. This differences between PA and attenuation spectra results in a continuously increasing LPCE with the increasing wavelength, from 70% to about 90%, with an uncertainty of ±6% on average.

The LHCE determined at 790 nm by the photoacoustic method were equal to 100% ± 3% and 78% ± 7% for γ-Fe₂O₃ and γ-Fe₂O₃–Au, respectively. We found a −22% difference compared to the +4% difference in Paściak *et al.* For our measurements, the difference could be explained by the enhanced scattering properties for γ-Fe₂O₃–Au compare to γ-Fe₂O₃. Interestingly for the photoacoustic coefficient that is mostly unsensitive to scattering, the concentration of Au NP in γ-Fe₂O₃–Au could be retrieved by spectral decomposition. The variation of the LHCE over the investigated wavelength range were found to be monotonous.

2.3. Advantage and limits for the determination of the LHCE with photoacoustic spectrometry

The main advantages of photoacoustic spectrometry for the determination of the LHCE are its ability to obtain multi-wavelength evaluation of LHCE on the same sample and within one experiment, its small uncertainty and the limited volume of solution required for the measurement. The multi-wavelength evaluation is made possible with the use of a tunable nanosecond pulsed laser and the photoacoustic spectra was acquired in four tubes in parallel in less than 30 seconds per acquisition. For methods based on the monitoring of the temperature for an illuminated solution, multiple continuous lasers are required to perform multi-wavelength acquisitions. Moreover, each acquisition last a few minutes to tens of minutes.[4] The uncertainty of our determination of the LHCE is on the order of 3% to 7%. This uncertainty is low because of

Fig. 4 Photoacoustic and attenuation spectra ((a), (c) and (e)) and Light-to-Photoacoustic Conversion Efficiency (LPCE, (b), (d) and (f)) for the maghemite nanoflowers (γ-Fe₂O₃), the gold nanoparticles (Au NP) and the maghemite nanoflowers decorated with gold nanoparticles (γ-Fe₂O₃–Au), respectively. The photoacoustic coefficients θ^{PA} were obtained with a calibrated photoacoustic spectrometer. Here, θ^{PA} is assumed to be equal to the photothermal conversion efficiency multiplied by the absorption coefficient of the dispersed phase. The attenuation coefficient $\mu_{att,\ dispersed}(\lambda)$ is measured with a spectrophotometer. The LPCE is the ratio of θ^{PA} to $\mu_{att,\ dispersed}(\lambda)$. For the photoacoustic coefficients, the median ± median absolute deviation values were displayed with dot markers and error bars. For the LPCE, the error bars correspond to the relative uncertainty and consider all the measurement and calibration steps. The axis ranges for the LCPE were 40%.

Paper

Nanoscale

the reproducibility of the measurements and the ability to perform 12 measurements on the same sample to compute median values. The volume of solution required for the 12 measurements is on the order of 500 µL. Each tube as a volume of 15 µL but the injection process is not fully optimized. The same volume can be used for the evaluation of the attenuation coefficient with a spectrophotometer. For comparison, a volume of a few mL is required for temperature monitoring in a cuvette and a few tens of µL can be used for methods with a hanging droplet. We previously determined that solutions with an absorption coefficient as low as 0.3 cm^{-1} can be measured with the photoacoustic spectrometer.[9] Here a photoacoustic coefficient of 0.24 cm^{-1} was measured at 920 nm for Ag$_2$S@DTDTPA, although we targeted solution with optical attenuation around 2 cm^{-1} to 4 cm^{-1} (absorbance of 1 to 2 for a 1 cm length cuvette). The optical absorption coefficient of water[11] $\mu_{a,\,water}(\lambda)$ varies from 5×10^{-3} cm^{-1} at $\lambda = 690$ nm to 0.1 cm^{-1} at 920 nm, therefore in addition to being subtracted by the blank acquisition, the absorption of the continuous phase could be neglected here for most of the measured solutions.

Compare to the macroscopic evaluations of the LHCE performed by considering the heat balance for a homogenized temperature in the sample compartment, photoacoustic spectrometry senses the heat transfer in the immediate vicinity of the particles, in particular for hard nanoparticles with a negligible thermal volume expansion. Probing the heating capabilities on a local scale before heat diffusion occurs and homogenize the temperature increase can be of interest to detect the capabilities to generate hot spots instead of a global hyperthermia. Local temperature increase has shown to enable photothermal effects inside biological cells specifically on lysosome membrane leading to enhanced cell necrosis of cancerous cells.[16] Thermo-responsive drug delivery systems incorporating photothermal agents could also benefit from a local heating.[17] At nanometric scale, numerical frameworks were proposed to simulate both the photothermal response and the photoacoustic signals for single nanoparticles illuminated by nanosecond pulses.[8,18,19] With a transition from single particles generating photoacoustic signals in the hundreds of MHz to solutions in tubes emitting in the MHz range, comparison between simulated photothermal properties and experimental measurements performed with the photoacoustic spectrometer would be of great interest and will be considered in a future study.

The photoacoustic evaluation of the photothermal properties of nanoparticles has a few limits. First, the Grüneisen coefficient of the solution may be different from that of the continuous phase. In the case of soft nanoparticles such as polymer nanoparticles for instance, the effective Grüneisen coefficient may combine the thermal volume expansion of both the nanoparticle and the continuous phase. A significant contribution of polymer nanoparticles to the effective Grüneisen coefficient has been observed when the constituting material had a thermal volumetric expansion coefficient larger than water and when a thermal confinement occurred at the length scale of the nanoparticles during the optical excitation.[20] Indeed, for short optical excitation (pulse width of

800 ps) which induce a heat confinement in polymer nanoparticles with a diameter larger than 100 nm, Aoki et al.[20] found that the effective Grüneisen coefficients of colloidal suspensions were larger than the Grüneisen coefficient of the continuous phase. In this case, the LPCE is no longer equivalent to the LHCE. For our photoacoustic spectrometer which operates with longer optical pulses (6–7 ns pulse width), the thermal confinement during the optical excitation is ensured for the spatial scale of the tube (solution compartment), but it is expected to be limited at the spatial scale of the nanoparticle; i.e. the characteristic length of the nanoparticle should be small compared to the thermal diffusion length in its constituting material. Consequently, the photoacoustic method presented here could be applicable for organic nanoparticles if the thermal expansion coefficient of their constituting material is low with respect to water and the thermal diffusivity is high. For continuous phases other than water, the current calibration procedure of the photoacoustic spectrometer should be adapted with the need to find new reference solutions in that solvent. Other than the Grüneisen coefficient, the pulsed optical excitation used in the photoacoustic spectrometer can have an influence compare to the continuous excitation of photothermal therapy when $E_{pt}(\lambda)$ depends on the illumination duration. This is true in particular when the optically absorbed energy can be stored by intermediate species or excited states living longer than the pulse but shorter than the thermal relaxation time. In this case, the LHCE will be underestimated with photoacoustic spectroscopy.

2.4. Discussion on the relevance of the LHCE

As shown by eqn (2), the LHCE as defined by Roper et al.[3] is sensitive to the scattering properties of the solution. The scattering properties of the photothermal nanoagents will impact the penetration of light in a suspension. However, when the nanoparticles are embedded in biological tissues for photothermal therapy, the scattering strength of the nanoagents may be considered negligible compared to the overall scattering induced by the tissue structures. Therefore, the photothermal conversion efficiency $E_{pt}(\lambda)$ is probably a better quantifier of the amount of optical energy that is converted into heat by the agents. The evaluation of $E_{pt}(\lambda)$ however requires the evaluation of the absorption coefficient from the attenuation coefficient, which can be challenging for scattering particles even with a spectrophotometer equipped with an integrating sphere.

Neither the LHCE nor the photothermal conversion efficiency include the absorption cross section of each particle. To really rank agents in terms of their capability to convert optical energy into heat, a more relevant metric could be the equivalent of the molar absorptivity coefficient. This quantity could be named molar or mass photothermal coefficient:

$$\zeta_T(\lambda) = E_{pt}(\lambda) \cdot \frac{\mu_a(\lambda)}{C_{dispersed}} \cong \frac{\theta^{PA}(\lambda)}{C_{dispersed}} \qquad (9)$$

where $C_{dispersed}$ is the molar or mass concentration of the dispersed phase. For nanoparticles, the mass concentration is often easier to determine than the molar concentration.

This molar or mass photothermal coefficient could be determined directly with photoacoustic spectrometry if the volume expansion of the nanoparticle can be neglected as for solid nanoparticles used as photothermal agents.

3. Conclusions

Calibrated photoacoustic spectroscopy was shown, both theoretically and experimentally, to provide a novel method for the determination of the Light-to-Heat Conversion Efficiency (LHCE) adapted to colloidal suspensions of solid nanoparticles. The method overcomes the limitations of the heat balance modelling, facilitates multi-wavelength determination of the LHCE and exhibits a low uncertainty.

The LHCE was determined to be equal to 100% for particles with weak luminescence and weak scattering properties, which is in line with a full transfer of the optically energy absorbed by the dispersed phase to the continuous phase in the form of heat. The lower LHCE values could be related to photothermal conversion efficiency reduced by the fluorescence quantum yield of the particles or to significant relative contribution of the scattering to the attenuation coefficient of the solution. The influence of the scattering on the LHCE value questions the relevance of this metric to characterize and compare photothermal nanoagents.

Calibrated photoacoustic spectroscopy could be used directly to obtain robust and accurate estimation of the photothermal properties of nanoagents with a mass photothermal coefficient that quantifies the three steps of photothermal therapy all together: optical absorption, thermal conversion of the absorbed energy and heat transfer to the surrounding medium.

4. Methods

4.1. Synthesis of the nanoparticles

4.1.1. Silver sulfide nanoparticles. Both $Ag_2S@MUA$ and $Ag_2S@DTDTPA$ Quantum Dots (QDots) were synthesized by precipitation and crystallization in aqueous media using microwave heating as reported in ref. 2. Briefly, $Ag_2S@MUA_{low}$ was prepared by mixing 5 mM (low concentration) of silver nitrate ($AgNO_3$) and 11-mercaptoundecanoic acid (11MUA) in the molar ratio 11MUA/Ag equal to 3, in 10 mL deionized (DI) water. The pH of the solution was adjusted to 8 using NH_3 (30%w) and HCL (37%w) and stirred for 24 h. Sodium Sulfide ($Na_2S·9H_2O$)(Ag/S: 2) was first dissolved in 4 mL DI water, then added to the reaction mixture just before microwave heating at 100 °C for 5 min (monomodal microwave Anton Paar Monowave 300, 300 W, 1200 tr min^{-1}). At the end of the reaction, QDots solution was precipitated using ethanol, centrifuged and then washed with DI water using a dialysis cassette (Thermo Scientific Slide-A-Lazer G2, 10 kDa) for 48 h. $Ag_2S@DTDTPA_{low}$ QDots were synthesized with the same procedure except to the ligand that is dithiolated diethyl-enetriamine pentaacetic acid (DTDTPA), and the molar ratio of DTDTPA/Ag/S: 1/2/1. No pH adjustment is necessary and the microwave temperature was set to 150 °C for 5 min. For QDots synthesis at the high concentration (20 mM of $AgNO_3$), the procedure has the same to low concentration with a microwave heating during 15 min. Characterization of Ag_2S samples are given in ESI Table S1 and Fig. S2† (TEM, mean size, hydrodynamic size, quantum yield).

4.1.2. Gold nanoparticles Au NP. The synthesis of Au@DTDTPA nanoparticles was based on the Brust method.[21] The reduction of the gold salt ($HAuCl_4·3H_2O$) was performed with sodium borohydride ($NaBH_4$) in the presence of a dithiolated derivative of diethylenetriaminepentaacetic acid (DTPA), named DTDTPA. The synthesis and characterization of the DTDTPA ligand was described earlier.[22,23]

For a typical preparation of gold nanoparticles, $HAuCl_4·3H_2O$ (200 mg, $51 × 10^{-5}$ mol) was placed in a 250 mL round-bottom flask and was dissolved with methanol (60 mL). In another flask, DTDTPA (256 mg, $50 × 10^{-5}$ mol), water (40 mL) and acetic acid (2 mL) were mixed. This solution containing DTDTPA was added to the gold salt solution under stirring. The mixture turned from yellow to orange. $NaBH_4$ (195 mg, $515 × 10^{-5}$ mol) dissolved in water (13.2 mL) was added to the gold–DTDTPA solution under stirring at room temperature. At the beginning of the $NaBH_4$ addition, the solution first became dark brown then a black flocculate appeared. The vigorous stirring was maintained for 1 h before adding aqueous hydrochloric acid solution (2 mL, 1 M). After the partial removal of the solvent under reduced pressure, the precipitate was retained on the polymer membrane and washed thoroughly and successively with 0.1 M hydrochloric acid, water and acetone. The resulting black powder was dried (up to 200 mg of dry powder of Au@DTDTPA) and dispersed in aqueous solution of sodium hydroxide (NaOH 0.01 M) to have a final concentration of 50 mM in gold.

The immobilization of Au@DTDTPA nanoparticles onto the maghemite nanoflowers requires the modification of the gold nanoparticles by dopamine. To obtain chelator-coated gold nanoparticles functionalized with dopamine (Au@DTDTPAd), an aqueous solution (3 mL) containing N-ethyl-N'-(3-dimethylaminopropyl) carbodiimide hydrochloride (EDC, 0.207 g; $1.08 × 10^{-3}$ mol) and N-hydroxysuccinimide (NHS, 0.247 g; $2.150 × 10^{-3}$ mol) was added to a suspension of Au@DTDTPA gold nanoparticles (6 mL, 50 mM). The suspension was stirred at pH 6 for 90 minutes. Afterwards, an aqueous solution (4 mL) containing dopamine ($9.45 × 10^{-3}$ g; $2.25 × 10^{-5}$ mol) was added to the suspension under stirring at pH 7.5. The mixture is stirred overnight. The purification of the suspension of gold nanoparticles was performed by dialysis against water (MWCO: 6–8 kDa) for 12 h. Water bath was changed three times every 3 h.

The measured suspension had a concentration of 1 g Au L^{-1}.

4.1.3. Maghemite nanoflowers γ-Fe_2O_3. Maghemite nanoflowers were first synthesized following the procedure published by Hugouenq et al.[24] $FeCl_3·6H_2O$ (2.164 g; 8 mmol) and $FeCl_2·4H_2O$ (0.795 g; 4 mmol) were completely dissolved

in diethylene glycol (DEG, 75 mL). The solution was stirred for one hour. The black-colored solution was poured with *N*-methyldiethanolamine (NMDEA, 75 mL) and stirred again for one hour. Separately, NaOH pellets (1.42 g; 35.6 mmol) were dissolved in a mixture of polyols (40 mL DEG and 40 mL NMDEA). This solution was added to the solution of iron chlorides and the resulting mixture was stirred for another three hours. Then, the temperature was elevated to 220 °C using a regular heating (2 °C min^{-1}). Once the temperature is set to 220 °C, the solution is stirred for 4 hours, and then cooled down slowly to room temperature by removing the heating plate. The black sediment was separated magnetically and washed with mixture of ethanol and ethyl acetate (1 : 1, v/v) for several times to eliminate organic and inorganic impurities. Possible iron hydroxides were removed by treatment with 10% nitric acid. Iron(III) nitrate (Fe(NO$_3$)$_3$·9H$_2$O) (2 g, 4.951 × 10^{-3} mol) is then dissolved in water (20 mL) and added to the nanoparticles. The resulting mixture is heated to 80 °C for 45 min to achieve a complete oxidation of the nanoparticles. After another treatment with 10% nitric acid, the particles were washed twice with acetone and diethyl ether and redispersed in water. At this stage, an aqueous dispersion of IONF is obtained that is stable in acid or basic conditions with a point of zero charge near pH 7.3.

The measured suspension had a concentration of 1.67 g Fe L^{-1}.

4.1.4. Maghemite nanoflowers decorated with gold nanoparticles γ-Fe$_2$O$_3$–Au. Maghemite nanoflowers decorated with gold nanoparticles were obtained by mixing under stirring the suspension of Au@DTDTPA modified by dopamine (Au@DTDTPAd) with the suspensions of maghemite nanoflowers (6 mL; 35 g Fe L^{-1}). The mixture with a pH of 5.5 was heated at 50 °C for 24 h. Successive washings were performed with ultrapure water, acetone, and diethyl ether until a clear supernatant was obtained. After purification the maghemite nanoflowers decorated with gold nanoparticles were introduced in ultrapure water at the desired concentration in iron. The measured suspension had a concentration of 1.67 g Fe L^{-1} and 0.3 g Au L^{-1}.

4.2. Spectrometers

4.2.1. Characterization of Ag$_2$S nanoparticle suspensions. Quantum yield (QY) of silver sulfite was measured using an Edinburgh FLS100 Spectrometer using deionized water as reference. The hydrodynamic sizes, zeta potentials, and polydispersity index (PDI) of the colloidal suspension of Ag$_2$S nanoparticles were assessed with a Zetasizer Nano ZS (Malvern Instruments, UK).

4.2.2. Characterization of maghemite nanoflowers. The hydrodynamic diameters (D_h) of AuNP, γ-Fe$_2$O$_3$ and Fe$_2$O$_3$–Au were measured using a Zetasizer Nano ZS (Malvern Instruments, UK) and are given Table S2.†

The concentration of gold and/or iron was determined with Inductively Coupled Plasma-Optical Emission Spectrometry (ICP-OES). The samples were mineralized in ultrapure aqua regia. An ICP-OES (710 ES Varian/Agilent) with axial torch with

a concentric nebulizer and cyclonic spray chamber was used. The parameters fixed during measurement were: power of 1.2 kW with argon auxiliary of 1.5 L min^{-1} and nebulizer pressure of 200 kPa. An ionizing buffer was employed for the measurements. The limit of detection of this technique is 20 μg L^{-1}.

4.2.3. Spectrophotometry. The attenuation coefficient of the colloidal nanoparticles in solution was measured with a spectrophotometer (VWR P4 Spectrophotometer, VWR, Leuven, Belgium) in absorbance mode using a 2 mm length quartz cuvette (QS 10.00 Hellma). The sample thickness was chosen to the avoid multiple scattering. The spectrophotometer was blanked with purified water (Milli-Q® IQ Water Purification System, Merk). The attenuation coefficient was obtained with eqn (3).

4.2.4. Photoacoustic spectrometry and analysis. The photoacoustic coefficient was measured with a calibrated photoacoustic (PA) spectrometer based on a conventional multispectral photoacoustic imaging system. The system has been described in details in ref. 9. For the sake of clarity, the main specifications are presented here. The sample solutions were injected in PTFE tubes (inner diameter: 0.2 mm, wall thickness: 0.1 mm, Bola, Germany), immersed in a water bath maintained at 25 °C. A thermostatic water bath (T100-ST12 Optima, Grant, UK) was used to monitor the water temperature during the whole experiment. The tubes were imaged successively at 30 optical wavelengths between 680 nm and 970 nm by steps of 10 nm. Optical excitation was generated by a tunable nanosecond laser (pulse width 6–7 ns) with a pulse repetition frequency of 20 Hz (SpitLight 600 OPO, Innolas Laser GmbH, Krailling, Germany). The laser fluence at 730 nm was around 2.5 mJ cm^{-2}. The ultrasound data were recorded with a linear ultrasound array (L7-4, ATL) driven by a programmable ultrasound machine (Vantage, Verasonics, WA, USA). The ultrasound signals were corrected for the pulse-to-pulse energy fluctuation of the laser and then averaged over 15 successive scans of the optical wavelengths before the image formation. Blank datasets were acquired by filling the tubes with water (Milli-Q® IQ Water Purification System, Merk) and were subtracted to the ultrasound signals for a baseline correction. Photoacoustic images were formed and the amplitude of the tube on the image was measured for each optical wavelength. This amplitude is named A^{PA}.

The calibration was performed with the reference solution of pentahydrate copper(II) sulfate (CuSO$_4$·5H$_2$O, ACS reagent, ≥98.0%, Sigma-Aldrich, St Louis, MO, USA) at 250 mM to convert A^{PA} in the PA coefficient $\theta^{PA}(\lambda)$. This solution is called the calibration solution.

$$\theta^{PA}(\lambda) = \frac{A^{PA}(\lambda)}{\tilde{A}^{PA}_{calibration}(\lambda)} \cdot \mu_a^{calibration}(\lambda) \cdot \eta_{PA}^{calibration} \quad (10)$$

where $\tilde{A}^{PA}_{calibration}(\lambda)$ is the median value of the amplitude A^{PA} for the calibration solution, $\mu_a^{calibration}(\lambda)$ is the absorption coefficient of the calibration solution, and $\eta_{PA}^{calibration}$ is the light-to-photoacoustic conversion efficiency (LPCE) for this calibration

solution. The LPCE coefficient is expected to be independent from the optical wavelength in the range 680 nm–970 nm since it is linked to the Grüneisen coefficient of the solution. The LPCE is determined by the injection of a solution of nigrosin, a black synthetic dye (Nigrosin, 198285, Sigma-Aldrich, St Louis, MO, USA) at 173 mg L^{-1}. The LPCE of the calibration solution was determined here to be: $\eta_{PA}^{calibration} = 1.274 \pm 0.008$ in the range 680 nm–920 nm (see ESI†).

The photoacoustic coefficient of the nanoparticles was measured in four tubes injected with the same solution simultaneously. The calibration was performed per tube. Typically, in a series of experiments, we performed two acquisitions with the calibration solution and one acquisition with the solution of nigrosin, between each sample. The calibration sequence was repeated at least 6 times for a robust estimation. For each sample, three acquisitions in four tubes were performed, leading to a total of 12 measurements per sample. The median of $\theta^{PA}(\lambda)$ was used as an estimate to avoid outliers due to possible injection errors. For the evaluation of the measurement error, we used the median absolute deviation with a scale factor 1.4826. The absorption of water increases above 920 nm and results in a degraded performance of our instrument, therefore, measurements performed for optical wavelengths above 920 nm were discarded.

The uncertainty of the estimation of the LPCE was developed in the ESI.†

Author contributions

J. G., T. L. and F. G. are responsible for the conceptualization of the project and experiments. T. L. and J. G. developed the methodology. T. L. and C. L. performed the photoacoustic and spectrophotometric measurements. T. L., C. L. and J. G. analysed and evaluated the data. L. A., T. N. and C. C. prepared and characterized the silver sulfide nanoparticles. M. H. characterized the suspension of silver sulfide nanoparticles. G. L., R. B. and S. R. prepared and characterized the maghemite nanoflowers and gold nanoparticles. All authors discussed and contributed to the preparation of the manuscript.

Conflicts of interest

There are no conflicts to declare.

Acknowledgements

References

1 K. Gu and H. Zhong, *Light: Sci. Appl.*, 2023, **12**, 120.

2 A. Paściak, R. Marin, L. Abiven, A. Pilch-Wróbel, M. Misiak, W. Xu, K. Prorok, O. Bezkrovnyi, L. Marciniak, C. Chanéac, F. Gazeau, R. Bazzi, S. Roux, B. Viana, V. P. Lehto, D. Jaque and A. Bednarkiewicz, *ACS Appl. Mater. Interfaces*, 2022, **14**(29), 33555–33566.

3 D. K. Roper, W. Ahn and M. Hoepfner, *J. Phys. Chem. C*, 2007, **111**, 3636–3641.

4 A. Paściak, A. Pilch-Wróbel, Ł. Marciniak, P. J. Schuck and A. Bednarkiewicz, *ACS Appl. Mater. Interfaces*, 2021, **13**, 44556–44567.

5 O. A. Savchuk, J. J. Carvajal, J. Massons, M. Aguiló and F. Díaz, *Carbon*, 2016, **103**, 134–141.

6 Y. Liu, P. Bhattarai, Z. Dai and X. Chen, *Chem. Soc. Rev.*, 2019, **48**, 2053–2108.

7 H. Zhu, B. Li, C. Yu Chan, B. Low Qian Ling, J. Tor, X. Yi Oh, W. Jiang, E. Ye, Z. Li and X. Jun Loh, *Adv. Drug Delivery Rev.*, 2023, **192**, 114644.

8 A. Prost, F. Poisson and E. Bossy, *Phys. Rev. B: Condens. Matter Mater. Phys.*, 2015, **92**, 1–16.

9 T. Lucas, M. Sarkar, Y. Atlas, C. Linger, G. Renault, F. Gazeau and J. Gateau, *Sensors*, 2022, **22**, 6543.

10 J. Weber, P. C. Beard and S. E. Bohndiek, *Nat. Methods*, 2016, **13**, 639–650.

11 K. F. Palmer and D. Williams, *J. Opt. Soc. Am.*, 1974, **64**, 1107–1110.

12 N. M. Anderson and P. Sekelj, *Phys. Med. Biol.*, 1967, **12**, 173–184.

13 Y. S. Chen, W. Frey, S. Aglyamov and S. Emelianov, *Small*, 2012, **8**, 47–52.

14 Y. Shen, H. D. A. Santos, E. C. Ximendes, J. Lifante, A. Sanz-Portilla, L. Monge, N. Fernández, I. Chaves-Coira, C. Jacinto, C. D. S. Brites, L. D. Carlos, A. Benayas, M. C. Iglesias-de la Cruz and D. Jaque, *Adv. Funct. Mater.*, 2020, **30**, 1–13.

15 A. Nicolás-Boluda, J. Vaquero, G. Laurent, G. Renault, R. Bazzi, E. Donnadieu, S. Roux, L. Fouassier and F. Gazeau, *ACS Nano*, 2020, **14**, 5738–5753.

16 A. Nicolas-Boluda, Z. Yang, T. Guilbert, L. Fouassier, F. Carn, F. Gazeau and M. P. Pileni, *Adv. Funct. Mater.*, 2021, **31**, 2006824.

17 D. Ghosh Dastidar and G. Chakrabarti, in *Applications of Targeted Nano Drugs and Delivery Systems*, Elsevier, 2019, pp. 133–155.

18 A. Hatef, B. Darvish, A. Dagallier, Y. R. Davletshin, W. Johnston, J. C. Kumaradas, D. Rioux and M. Meunier, *J. Phys. Chem. C*, 2015, **119**, 24075–24080.

19 N. Amjadi, A. Hatef and R. Malekfar, *J. Phys. Chem. C*, 2022, **126**, 20584–20593.

20 H. Aoki, M. Nojiri, R. Mukai and S. Ito, *Nanoscale*, 2015, **7**, 337–343.

21 M. Brust, J. Fink, D. Bethell, D. J. Schiffrin and C. Kiely, *J. Chem. Soc., Chem. Commun.*, 1995, 1655.

22 C. Alric, J. Taleb, G. Le Duc, C. Mandon, C. Billotey, A. Le Meur-Herland, T. Brochard, F. Vocanson, M. Janier, P. Perriat, S. Roux and O. Tillement, *J. Am. Chem. Soc.*, 2008, **130**, 5908–5915.

23 P.-J. Debouttière, S. Roux, F. Vocanson, C. Billotey, O. Beuf, A. Favre-Réguillon, Y. Lin, S. Pellet-Rostaing, R. Lamartine, P. Perriat and O. Tillement, *Adv. Funct. Mater.*, 2006, **16**, 2330–2339.

24 P. Hugounenq, M. Levy, D. Alloyeau, L. Lartigue, E. Dubois, V. Cabuil, C. Ricolleau, S. Roux, C. Wilhelm, F. Gazeau and R. Bazzi, *J. Phys. Chem. C*, 2012, **116**, 15702–15712.